

A half-step in quantized conductance for low-density electrons in a quantum wire

Godfrey Gumbs^{1,4,*} Antonios Balassis^{2,†} Danhong Huang^{3,‡} Sheehan Ahmed^{2,§} and Ryan Brennan^{2,¶}

¹*Department of Physics and Astronomy,
Hunter College of the City University of New York,
695 Park Avenue, New York, NY 10065, USA*

²*Physics Department, Fordham University,
441 East Fordham Road, Bronx, NY 10458, USA*

³*Air Force Research Laboratory, Space Vehicles Directorate,
Kirtland Air Force Base, NM 87117, USA and*

⁴*Donostia International Physics Center (DIPC), P. de Manuel Lardizabal,
4, 20018 San Sebastián, Basque Country, Spain*

(Dated: August 8, 2018)

Abstract

We investigated the effect due to perpendicular magnetic field on quantum wires where spin-orbit interaction (SOI) of electrons is not neglected. Based on the calculated energy dispersion, the nonlinear ballistic conductance (G) and electron-diffusion thermoelectric power (S_d) are calculated as functions of electron density, temperature and applied bias voltage. A low-temperature half-step feature in G , which was observed experimentally by Quay *et al.* [see Nature Physics **6**, 336 (2010)], as well as a new peak in S_d are reproduced here in the low density regime. These phenomena are related to the occurrence of the Zeeman splitting and SOI induced saddle point in the band structure, where the channel chemical potential lies within an anticrossing gap between the saddle point of the lower subband and the bottom of the upper subband. Additionally, side peaks in G far away from the zero bias for the nonlinear transport, as well as a quadratic bias-voltage dependence of G near zero voltage, are predicted and discussed.

I. INTRODUCTION

Quasi-one-dimensional (quasi-1D) electron systems (also called quantum wires) have attracted considerable attention both theoretically¹⁻³ and experimentally^{4,5} since their experimental realization in 1986.⁶ When an external magnetic field is applied in a direction perpendicular to a quantum wire, Landau quantization in such a system combines with lateral confinement, enhancing the quantum-wire confinement potential as well as the effective mass of electrons along the wire direction at the same time.^{7,8} Several studies were reported for such systems, including magneto-optical properties^{5,9} and magneto-transport properties¹⁰⁻¹⁵ in the diffusive regime. Moreover, the ballistic transport properties¹⁶⁻¹⁸ of quantum wires were also explored under a tilted magnetic field.

On the other hand, the effect of Rashba spin-orbit interaction (SOI) on the ballistic and diffusive electron transport properties in quantum wires has also been investigated theoretically and experimentally in the absence of a magnetic field.¹⁹⁻²³ Compared with the case when SOI is neglected,²⁴ the quantum-wire conductance quantization in the presence of SOI is modified significantly at low temperatures.²³ Although the SOI-induced gap has been observed experimentally,²⁵ there are only a few theoretical studies dealing with ballistic electron transport and thermoelectric properties in parabolically-confined quantum wires with both SOI and a magnetic field.²⁶⁻²⁸

In this paper, we include the effects due to the edges of a realistic quantum wire through sharp and high potential walls forming the boundaries, instead of assuming a parabolic potential for the lateral confinement of the quantum-wire. Extending our previous study for zero magnetic field in the linear response regime,²³ we calculate the bias-voltage dependent nonlinear ballistic conductance and electron-diffusion thermoelectric power for this quasi-one-dimensional system with a channel length less than the electron mean free path, where we have included the effect on the SOI of a finite magnetic field perpendicular to the quantum wire as well as the Zeeman effect on the electron spin states. A half-step feature in the quantized conductance is obtained for low electron densities and low temperatures.

The rest of this paper is arranged as follows. In Sec. II, we present our model for quantum wires with SOI under a perpendicular magnetic field. Numerical results and discussion of the energy bands, conductance and diffusion thermoelectric power as functions of electron

density, temperature and bias voltage are presented in Sec. III. We summarize our results in Sec. IV.

II. THE MODEL

In the presence of a magnetic field \mathbf{B} (in the z direction) perpendicular to a quantum wire which is confined in the x direction such that $|x| \leq \mathcal{W}/2$ and extends along the y direction, the spin-coupled Schrödinger equations for the electron wave-function spinor, $[\psi_{k_y}^\uparrow(x), \psi_{k_y}^\downarrow(x)]^T$, with the Landau gauge are written as²³

$$\begin{aligned} & -\frac{\hbar^2}{2m^*} \left[\frac{d^2}{dx^2} - \left(k_y + \frac{x}{\ell_c^2} \right)^2 \right] \psi_{k_y}^\uparrow(x) + \alpha \left[\frac{d}{dx} + \left(k_y + \frac{x}{\ell_c^2} \right) \right] \psi_{k_y}^\downarrow(x) \\ & - \beta \frac{\mathcal{W}}{\ell_0} \left(k_y + \frac{x}{\ell_c^2} \right) \mathcal{F}(x) \psi_{k_y}^\uparrow(x) = \left(\varepsilon - \frac{1}{2} g^* \hbar \omega_c \right) \psi_{k_y}^\uparrow(x), \end{aligned} \quad (1)$$

$$\begin{aligned} & -\frac{\hbar^2}{2m^*} \left[\frac{d^2}{dx^2} - \left(k_y + \frac{x}{\ell_c^2} \right)^2 \right] \psi_{k_y}^\downarrow(x) - \alpha \left[\frac{d}{dx} - \left(k_y + \frac{x}{\ell_c^2} \right) \right] \psi_{k_y}^\uparrow(x) \\ & + \beta \frac{\mathcal{W}}{\ell_0} \left(k_y + \frac{x}{\ell_c^2} \right) \mathcal{F}(x) \psi_{k_y}^\downarrow(x) = \left(\varepsilon + \frac{1}{2} g^* \hbar \omega_c \right) \psi_{k_y}^\downarrow(x), \end{aligned} \quad (2)$$

where β and α are the SOI parameters in the transverse x and z directions, respectively. Also, ε is the eigenenergy of the electrons, the symbols \uparrow and \downarrow denote the up and down spin states, k_y is the electron wave number along the wire, m^* is the effective mass, $\omega_c = eB/m^*$ is the cyclotron frequency, $\ell_c = \sqrt{\hbar/eB}$ is the magnetic length, and g^* is the effective Lande spin g -factor. Additionally, the quantum confinement factor²³ introduced in the above equations for a non-parabolic confinement is given by

$$\mathcal{F}(x) = \exp \left[-\frac{(x + \mathcal{W}/2)^2}{2\ell_0^2} \right] - \exp \left[-\frac{(x - \mathcal{W}/2)^2}{2\ell_0^2} \right], \quad (3)$$

where ℓ_0 describes the steepness of the confinement potential at the two edges of the wire. Compared with the case of $B = 0$,²³ we see that k_y is replaced by $(k_y + x/\ell_c^2)$, as well as the appearance of a Zeeman splitting term, in Eqs. (1) and (2) when $B \neq 0$.

For ballistic electrons in a quantum wire, the charge ($n = 0$) and the heat ($n = 1$) currents are calculated as²⁴

$$\begin{aligned} \mathcal{Q}^{(n)}(V_b) &= (-e)^{1-n} \frac{1}{2\pi} \sum_j \int_{-\infty}^{\infty} dk_y (\varepsilon_{jk_y} - \mu_c) v_{jk_y} \\ &\times \left[\theta(-v_{jk_y}) f_{jk_y}^{(R)} (1 - f_{jk_y}^{(L)}) + \theta(v_{jk_y}) f_{jk_y}^{(L)} (1 - f_{jk_y}^{(R)}) \right]. \end{aligned} \quad (4)$$

In this notation, $j = 1, 2, \dots$ is a composite index labeling the spin-resolved subbands, $v_{jk_y} = (1/\hbar) d\varepsilon_{jk_y}/dk_y$ is the group velocity of electrons in the j th subband, $\theta(x)$ is the unit step function, μ_c is the chemical potential of the quantum wire, $f_{jk_y}^{(s)} = \{1 + \exp[(\varepsilon_{jk_y} - \mu_s)/k_B T]\}^{-1}$, T is the temperature of the system, $s = R, L$ denotes the right and left electrodes connected to two ends of a quantum wire in the y direction, $\mu_L = \mu_c - eV_b/2$ and $\mu_R = \mu_c + eV_b/2$ represent the chemical potentials of the left and right electrodes, satisfying $\mu_R - \mu_L = eV_b$ with V_b being the external bias voltage. For fixed chosen linear electron density n_{1D} and T , μ_c can be calculated using the following constraint equation

$$\sum_j \left\{ \int_{-\infty}^{\infty} \frac{dk_y}{\exp[(\varepsilon_{jk_y} - \mu_c)/k_B T] + 1} \right\} - 2\pi n_{1D} = 0. \quad (5)$$

Once the $\mathcal{Q}^{(n)}(V_b)$ in Eq. (4) has been calculated, the bias-dependent ballistic conductance $G(V_b)$ of the quantum wire is simply given by

$$G(V_b) = \frac{\mathcal{Q}^{(0)}(V_b)}{V_b}, \quad (6)$$

and the diffusion thermoelectric power $S_d(V_b)$ may be calculated according to

$$S_d(V_b) = \frac{1}{T} \left[\frac{\mathcal{Q}^{(1)}(V_b)}{\mathcal{Q}^{(0)}(V_b)} \right]. \quad (7)$$

We now employ these quantities to carry out our numerical calculations.

III. NUMERICAL RESULTS

In our calculations, we define two spin-related characteristic lengths, namely, $\ell_\alpha = \hbar^2/(2m^*\alpha)$ and $\ell_\beta = \hbar^2/(2m^*\beta)$. Consequently, four corresponding dimensionless quantities related to spin-orbit coupling, quantum confinement factor and magnetic-field effect are given by: $\tau_\alpha = \mathcal{W}/\ell_\alpha \propto \alpha$, $\tau_\beta = \mathcal{W}/\ell_\beta \propto \beta$, $\tau_0 = \mathcal{W}/\ell_0$ and $\tau_c = \mathcal{W}/\ell_c \propto \sqrt{B}$. The scaled electron kinetic energy is ε_{jk_y}/E_0 with $E_0 = \pi^2\hbar^2/2m^*\mathcal{W}^2$, the scaled electron wave

number is $k_y\mathcal{W}$, and the scaled position variable is x/\mathcal{W} . Parameters in our calculations were chosen as $m^* = 0.067 m_0$ (as in GaAs) with m_0 being the free-electron mass, $g^* = -0.44$ due to exchange interaction, $\tau_\beta = 10$, $\mathcal{W} = 568.7 \text{ \AA}$ and $\tau_0 = 10^3$. Other parameters, such as τ_α , B , T , V_b and n_{1D} , will be given in the figure captions.

Figure 1 shows the calculated eigenenergy ε_{jk_y}/E_0 as a function of $k_y\mathcal{W}$ for three different cases, i.e., (a) $\tau_\alpha = 10$, $B = 0 \text{ T}$; (b) $\tau_\alpha = 10$, $B = 1 \text{ T}$; (c) $\tau_\alpha = 0$, $B = 1 \text{ T}$. From Fig. 1(a), we find that the spin-orbit interaction under $\alpha \neq 0$ couples spin-up and spin-down electron states in the absence of a B field. Here, the energy dispersion curves of the spin-up and spin-down states are shifted relative to each other with respect to $k_y = 0$. In the presence of a B field, as shown in Fig. 1(b), many anticrossing gaps are created due to both Zeeman splitting and SOI, the effective mass of electrons along the wire is enhanced, and new saddle points are formed.¹³ After the spin-orbit interaction is turned off, we simply see a set of Zeeman split parabolas, as demonstrated by Fig. 1(c). When $B \rightarrow \infty$, these subbands will convert into discrete Landau levels (with infinite effective mass along the y direction).

The results for the quantum-wire chemical potential μ_c/E_0 , the ballistic conductance G [in units of (e^2/h)], and the diffusion thermoelectric power S_d [in units of $(-k_B/e)$] are compared in Figs. 2(a), (b) and (c), respectively, for the three cases discussed in Fig. 1. Here, $T = 4 \text{ K}$ and a small bias voltage $V_b = 0.1 \text{ meV}$ is used for the linear-response regime. From Fig. 2(a) we see that when $\alpha \neq 0$, μ_c is reduced at high electron densities but enhanced at low densities by the B field due to the formed anticrossing gap and increased electron effective mass. Additionally, there exists a series of kinks in μ_c as a function of n_{1D} , which is related to the onset of a new subband population. By turning off the SOI, μ_c is increased for finite values of B and the kinks in μ_c are shifted at the same time due to the suppression of the flattened region around $k_y = 0$ where the density of states is expected to be high. This series of kinks observed in Fig. 2(a) leads to the occurrence of quantum steps for G in Fig. 2(b). Furthermore, each quantum step in G relates to a peak in S_d , as presented in Fig. 2(c). It is interesting to note that the application of the B field has a very profound effect on the spin-orbit interaction of electrons at low densities, where a new step (indicated by a black arrow) in (b) and a new peak in (c) are seen in correspondence to μ_c lying inside the lowest anticrossing gap. Similar half-step features were observed experimentally.²⁵

Comparisons for μ_c , G and S_d as a function of temperature T for the three cases discussed

in Fig. 1 are presented in Figs. 3(a), (b) and (c), respectively, where we chose $n_{1D} = 10^6 \text{ cm}^{-1}$ and $V_b = 0.1 \text{ meV}$. With a finite SOI, the B field reduces (increases) μ_c in Fig. 3(a) for $T < 4 \text{ K}$ ($T > 4 \text{ K}$). For $\alpha = 0$, μ_c is significantly enhanced. Meanwhile, μ_c , which lies within the gap of the second and third parabolas, increases with T in contrast to the case when $\alpha \neq 0$ where a decreasing μ_c with T is obtained due to the fact that μ_c stays very close to the two minima of the third subband in Figs. 1(a) and (b). For nonzero SOI, G increases with T in Fig. 3(b) as a result of the gradual thermal population of higher subbands slightly above μ_c . On the other hand, G is decreased when T is increased in the absence of spin-orbit coupling since $G \propto [-\partial f_{jk_y}^{(s)}/\partial \varepsilon_{jk_y}]$ whose peak strength is reduced by increasing T provided μ_c lies within a gap. In addition, as can be seen from Fig. 3(c), S_d monotonically increases with T , and becomes linearly proportional to T above 4 K .¹⁴ However, it becomes exponentially small for $T \ll 1 \text{ K}$.¹⁴ For $\alpha = 0$, S_d becomes much smaller than in the previous two cases due to a larger value of G .

We present in Fig. 4 comparisons between the bias voltage (V_b) dependence of G in (a), the low-voltage blow-out view of Fig. 4(a) in (b) and the charge current $\mathcal{Q}^{(0)}$ in (c) for the three cases considered in Fig. 1, where $n_{1D} = 10^6 \text{ cm}^{-1}$ and $T = 4 \text{ K}$. When $\tau_\alpha = 10$ in Fig. 4(a), G initially increases with $|V_b|$ from $2e^2/h$ in a symmetric way, which is followed by a decrease before it increases again. The B field does not alter the shape of the $G - V_b$ curve except for a small reduction of G . On the other hand, G decreases with $|V_b|$ from $4e^2/h$ and eventually saturates at $3e^2/h$ for $\tau_\alpha = 0$. These dramatically distinct behaviors in G are attributed to different positions of the chemical potentials in the two electrodes relative to the bottom of subbands as $V_b \rightarrow 0$, as explained in Fig. 3. In order to see the behavior of G in the low-voltage regime, we display in Fig. 4(b) the blow-out view of Fig. 4(a), where a quadratic dependence of G on V_b can be identified. Figure 4(c) exhibits a different dependence of $\mathcal{Q}^{(0)}$ on V_b . For the cases with $\tau_\alpha = 10$, the leading term in the charge current is $\mathcal{Q}^{(0)} \propto V_b [-\partial f_{jk_y}^{(s)}/\partial \varepsilon_{jk_y}]$ for $|V_b| \leq 1.5 \text{ meV}$. However, for $|V_b| \geq 2.5 \text{ meV}$ in Fig. 4(c), we find that the leading term changes to $\mathcal{Q}^{(0)} \propto V_b^3 [-\partial^3 f_{jk_y}^{(s)}/\partial \varepsilon_{jk_y}^3]$. This explains the observations in Fig. 4(b), i.e., $G = 2e^2/h$ for $V_b \rightarrow 0$ (linear response) and $G \propto V_b^2$ (nonlinear response) for large values of $|V_b|$. As $\tau_\alpha = 0$, the slope in the linear-response regime is greatly enhanced because of a larger value of the Fermi velocity (large μ_c), leading to a quadratic decrease of G with V_b in Fig. 4(b) as $|V_b|$ increases.

In Fig. 5 we display two-dimensional (2D) contour plots of $G(n_{1D}, T)$ in (a) and (b) as well as 2D contour plots of $S_d(n_{1D}, T)$ in (c) and (d) when $B = 0$ [(a) and (c)] and when $B = 1$ T [(b) and (d)]. We chose $V_b = 0.1$ meV and $\tau_\alpha = 10$. In general, for both $B = 0$ and $B = 1$ T, we clearly see quantized steps in G and peaks in S_d with increasing n_{1D} at any value of T in this figure. The step and peak positions are almost independent of T . However, in the low-density regime when $n_{1D} \leq 0.5 \times 10^6 \text{ cm}^{-1}$, the presence of the B field modifies the spin-orbit coupling and dramatically alters the behaviors of G and S_d as functions of both n_{1D} and T .

We compare the 2D contour plots of $G(T, V_b)$ in Fig. 6 at $B = 0$ in (a) and $B = 1$ T in (b), for chosen $n_{1D} = 10^6 \text{ cm}^{-1}$ and $\tau_\alpha = 10$. It is easy to see that the two strong peaks in G on either side of $V_b = 0$ are greatly suppressed by the magnetic field, which is further accompanied by an expanded dip around $V_b = 0$. In addition, the peaks in G decrease with T .

For completeness, we present in Fig. 7 the 2D contour plots of $G(n_{1D}, V_b)$ for $B = 0$ and $B = 1$ T in (a) and (b), respectively, at $T = 4$ K when $\tau_\alpha = 10$. It is clear that the quantized steps in G become most observable close to $V_b = 0$. The B field does not significantly affect G in the high-density regime ($n_{1D} \geq 2.5 \times 10^6 \text{ cm}^{-1}$). In the intermediate-density regime ($1.2 \times 10^6 \text{ cm}^{-1} \leq n_{1D} \leq 2.5 \times 10^6 \text{ cm}^{-1}$), G only weakly depends on $|V_b|$ and shows no B -field effect. In the low-density regime ($n_{1D} \leq 1.2 \times 10^6 \text{ cm}^{-1}$), however, the B field changes G substantially as functions of both n_{1D} and $|V_b|$. The dip around $V_b = 0$ evolves into a peak and vice versa with increasing n_{1D} due to the variation of the relative position of μ_c with respect to the bottom of the subband.

IV. SUMMARY AND CONCLUDING REMARKS

In summary, we have investigated the combined effect of SOI and an external magnetic field which is applied perpendicularly to a quantum wire. The quantities calculated are the the quasi-one-dimensional energy subbands, the nonlinear ballistic conductance (G) and electron-diffusion thermoelectric power (S_d) as functions of electron density, temperature and applied bias voltage. An important outcome of our numerical calculations is the observation of a half-step in the low-temperature quantized conductance at low electron densities. We have accounted for this feature as being due to the occurrence of a saddle point in the

subband energy dispersion relation. The saddle point is due to the combined action of the applied magnetic field and spin-orbit coupling in the wire. A similar low-temperature half-step feature in G was observed experimentally by Quay *et al.*²⁵. A new peak in S_d is produced in the low density regime, and is also related to the occurrence of the magnetic field and SOI induced saddle point in the band structure, where the channel chemical potential lies within an anticrossing gap between the saddle point of the lower subband and the bottom of the upper subband. Additionally, the present nonlinear transport theory has predicted side peaks in the quantized conductance as a function of bias voltage away from zero and a quadratic bias dependence near zero voltage. This extension of our previous work²³ clearly demonstrates that the application of magnetic field leads to observable differences in the ballistic transport properties of a quantum wire structure with SOI playing a role.

Acknowledgments

This research was supported by contract # FA 9453-11-01-0263 of AFRL. DH would like to thank the Air Force Office of Scientific Research (AFOSR) for its support.

* Electronic address: ggumbs@hunter.cuny.edu

† Electronic address: balassis@fordham.edu

‡ Electronic address: danhong.huang@kirtland.af.mil

§ Electronic address: ashahmed@fordham.edu

¶ Electronic address: rybrennan@fordham.edu

¹ Q. P. Li and S. Das Sarma, Phys. Rev. B **43**, 11768 (1991).

² G. Gumbs, D. H. Huang, Y. Yin, H. Qiang, D. Yan, F. H. Pollak and T. F. Noble, Phys. Rev. B **48** 18328 (1993).

³ G. Gumbs and D. H. Huang, *Properties of Interacting Low-Dimensional Systems*, (Wiley-VCH Verlag GmbH & Co. KGaA, Weinheim, Germany, 2011), p. 275 and p. 303.

⁴ W. Hansen, M. Horst, J. P. Kotthaus, U. Merkt, Ch. Sikorski and K. Ploog, Phys. Rev. Lett. **58**, 2586 (1987).

⁵ T. Demel, D. Heitmann, P. Grambow and K. Ploog, Phys. Rev. B **38**, 12732 (1988).

- ⁶ T. J. Thornton, M. Pepper, H. Ahmed, D. Andrews, and G. J. Davies, Phys. Rev. Lett. **56**, 1198 (1986).
- ⁷ H. L. Stormer, L. N. Pfeiffer, K. W. Baldwin, K. W. West and J. Spector, Appl. Phys. Lett. **58**, 726 (1991).
- ⁸ G. Gumbs, D. H. Huang and D. Heitmann, Phys. Rev. B **44**, 8084 (1991).
- ⁹ D. H. Huang, G. Gumbs and N. J. M. Horing, Phys. Rev. B **49**, 11463 (1994).
- ¹⁰ D. Weiss, K. von Klitzing, K. Ploog and G. Weimann, Europhys. Lett. **8**, 179 (1989).
- ¹¹ C. Zhang and R. R. Gerhardts, Phys. Rev. B **41** 12850 (1990).
- ¹² D. H. Huang and S. K. Lyo, J. Phys.: Condens. Matter **12**, 3383 (2000).
- ¹³ S. K. Lyo and D. H. Huang, Phys. Rev. B **64** 115320 (2001).
- ¹⁴ S. K. Lyo and D. H. Huang, Phys. Rev. B **66** 155307 (2002).
- ¹⁵ S. K. Lyo and D. H. Huang, Phys. Rev. B **68** 115317 (2003).
- ¹⁶ S. F. Fischer, G. Aeppli, U. Kunze, D. Schuh and G. Abstreiter, Nat. Phys. **2**, 91 (2006); Phys. Rev. B **74**, 115324 (2006).
- ¹⁷ Lev G. Mourokh, A. Yu. Smirnov and S. F. Fischer, Appl. Phys. Lett. **90**, 132108 (2007).
- ¹⁸ D. H. Huang, S. K. Lyo, K. J. Thomas and M. Pepper, Phys. Rev. B **77**, 085320 (2008).
- ¹⁹ A. V. Moroz, K. V. Samokhin and C. H. W. Barnes, Phys. Rev. Lett. **84**, 4164 (2000).
- ²⁰ A. V. Moroz and C. H. W. Barnes, Phys. Rev. B **60**, 14272 (1999).
- ²¹ Y. V. Pershin, J. A. Nesteroff, and V. Privman, Phys. Rev. B **69**, 121306 (2004).
- ²² G. Gumbs, Phys. Rev. B **70**, 235314 (2004).
- ²³ G. Gumbs, A. Balassis and D. H. Huang, J. Appl. Phys. **108**, 093704 (2010).
- ²⁴ S. K. Lyo and D. H. Huang, J. Phys.: Condens. Matter **16**, 3379 (2004).
- ²⁵ C. H. L. Quay, T. L. Hughes, J. A. Sulpizio, L. N. Pfeiffer, K. W. Baldwin, K. W. West, D. Goldhaber-Gordon, and R. de Picciotto, Nat. Phys. **6**, 336 (2010).
- ²⁶ S. DeBald and B. Kramer, Phys. Rev. B **71**, 115322 (2005).
- ²⁷ T.-Y. Zhang, W. Zhao and X.-M. Liu, J. Phys.: Condens. Matter **21**, 335501 (2009).
- ²⁸ H.-F. Lü, L.-C. Zhu, X.-T. Zu and H.-W. Zhang, Appl. Phys. Lett. **96**, 123111 (2010).

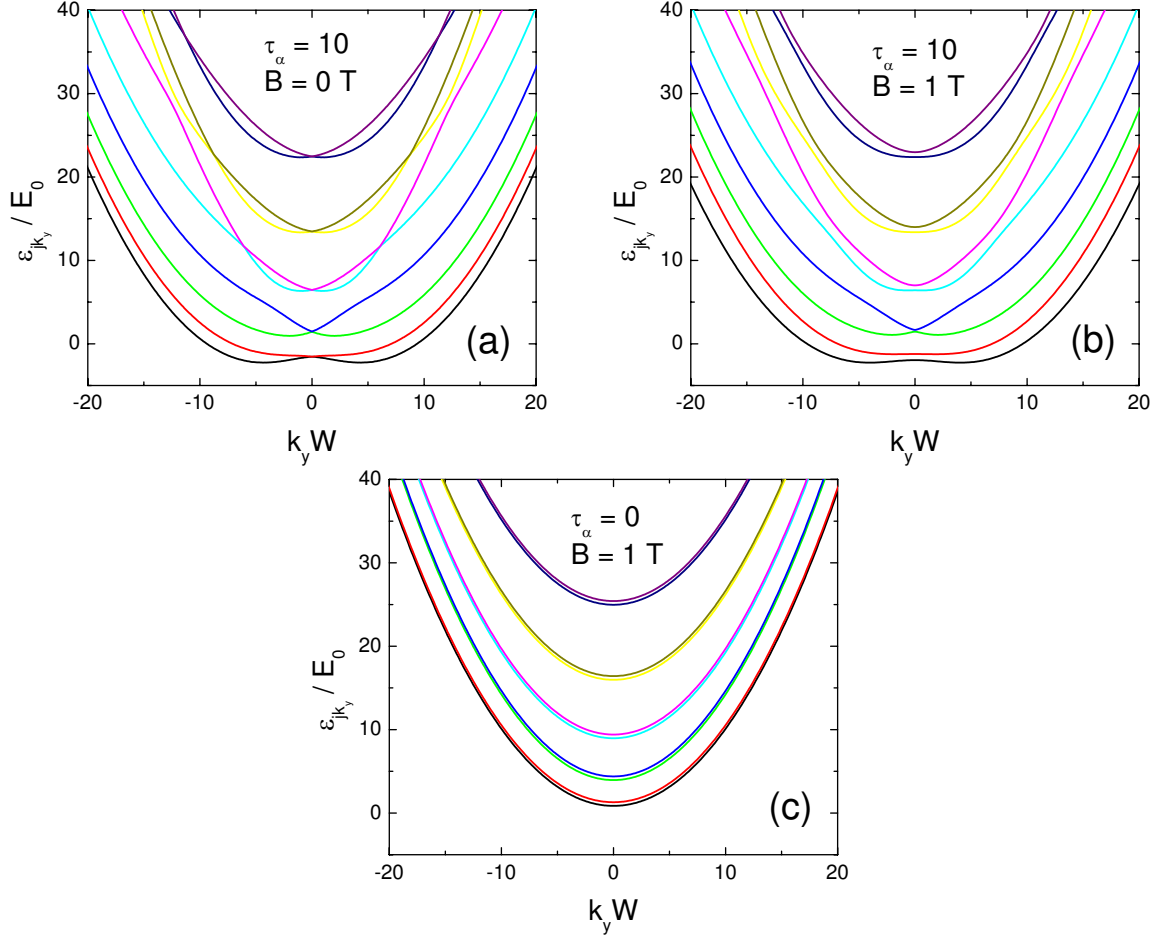


FIG. 1: (Color online) The calculated eigenenergies ε_{jk_y}/E_0 as functions of $k_y W$ for the three cases considered: (a) $\tau_\alpha = 10$ and $B = 0$ T; (b) $\tau_\alpha = 10$ and $B = 1$ T; (c) $\tau_\alpha = 0$ and $B = 1$ T. The Zeeman splitting in (c) can be resolved for $B = 1$ T. The degeneracy of \uparrow and \downarrow spin states at $k_y = 0$ are split by the Zeeman effect in (b) to form an anticrossing gap.

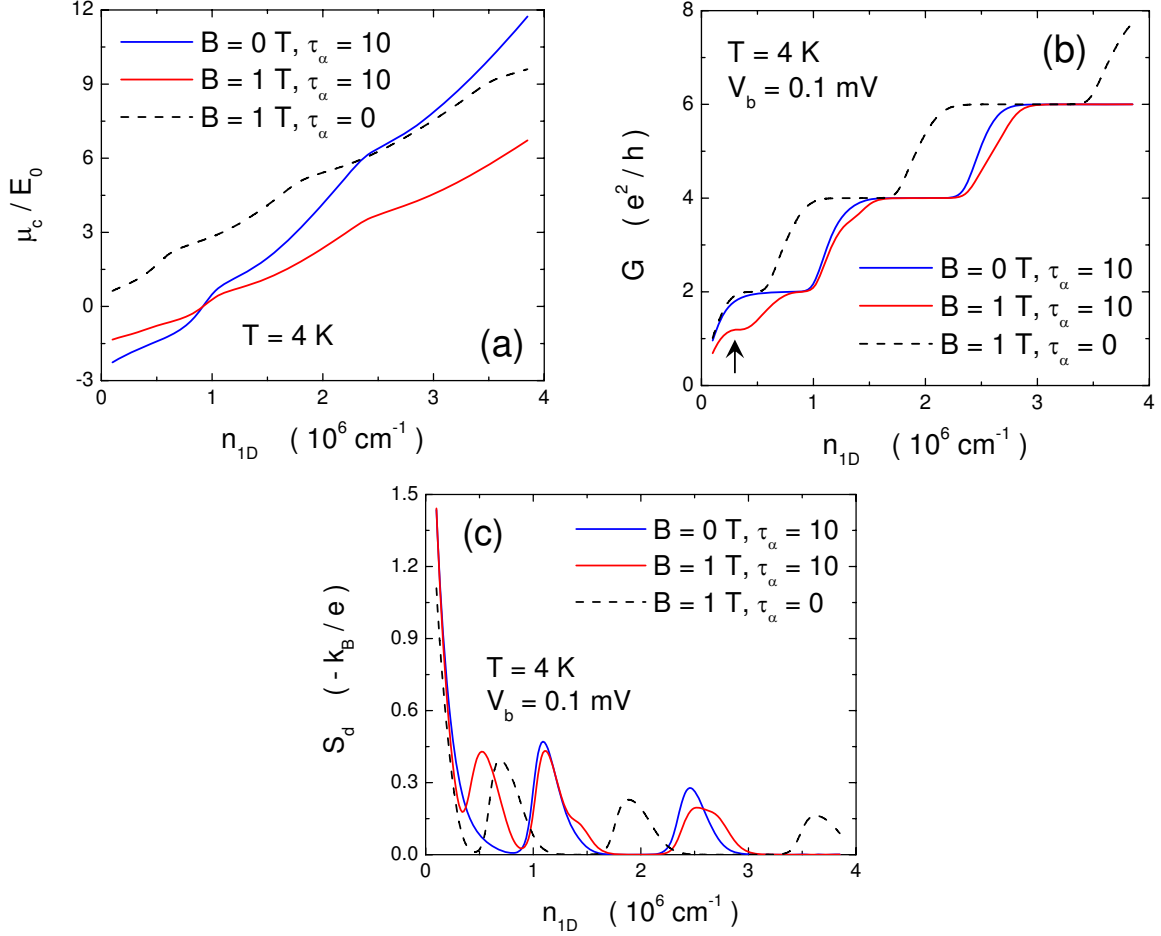


FIG. 2: (Color online) (a) Chemical potential μ_c (in units of E_0) for a quantum wire, (b) ballistic conductance G (in units of (e^2/h)) and (c) diffusion thermoelectric power S_d (in units of $(-k_B/e)$) as functions of the linear density n_{1D} for the three cases: $\tau_\alpha = 10$, $B = 0 \text{ T}$ (blue solid curves); $\tau_\alpha = 10$, $B = 1 \text{ T}$ (red solid curves); and $\tau_\alpha = 0$, $B = 1 \text{ T}$ (black dashed curves), where $T = 4 \text{ K}$ and $V_b = 0.1 \text{ meV}$. The black arrow in (b) indicates a half-step in quantized conductance G .

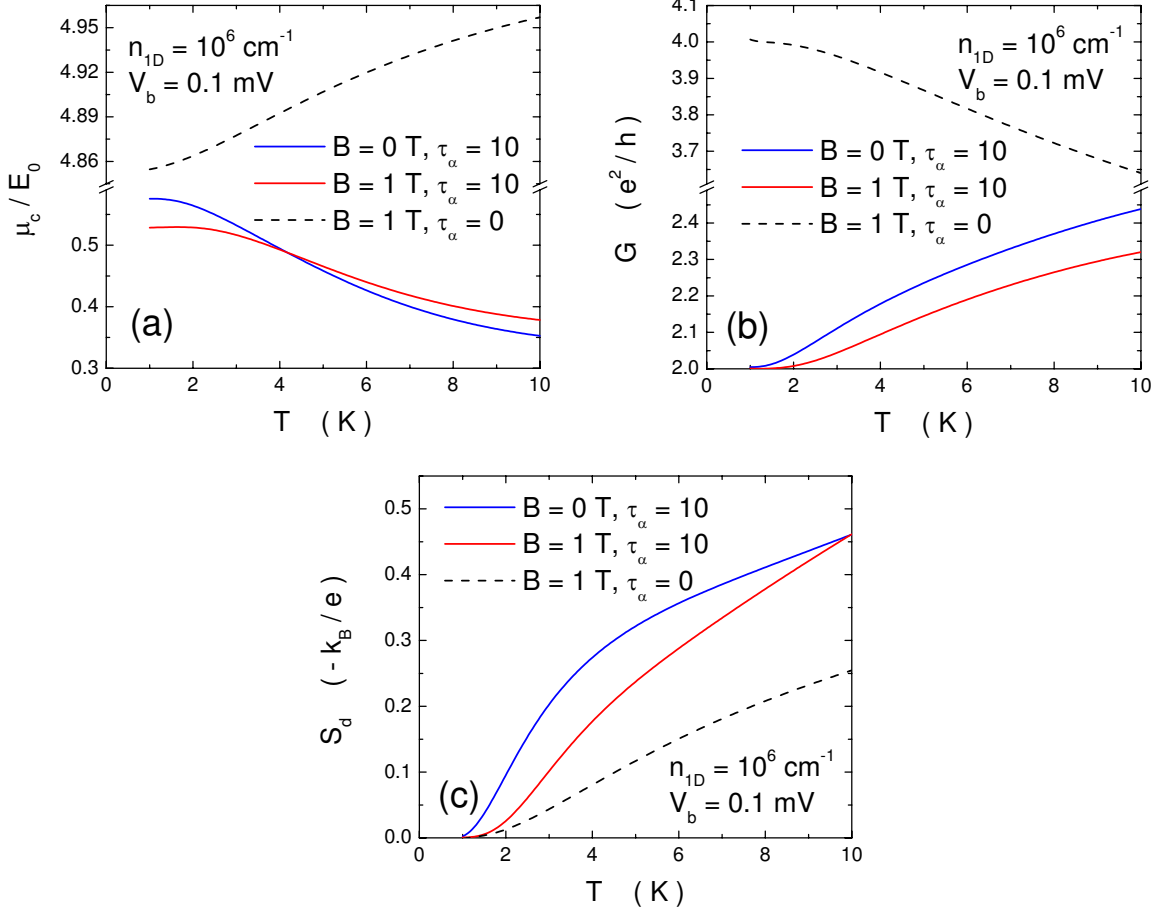


FIG. 3: (Color online) Calculated (a) μ_c , (b) G and (c) S_d as functions of temperature T for the three cases: $\tau_\alpha = 10$, $B = 0 \text{ T}$ (blue solid curves); $\tau_\alpha = 10$, $B = 1 \text{ T}$ (red solid curves); and $\tau_\alpha = 0$, $B = 1 \text{ T}$ (black dashed curves), where $n_{1D} = 10^6 \text{ cm}^{-1}$ and $V_b = 0.1 \text{ meV}$.

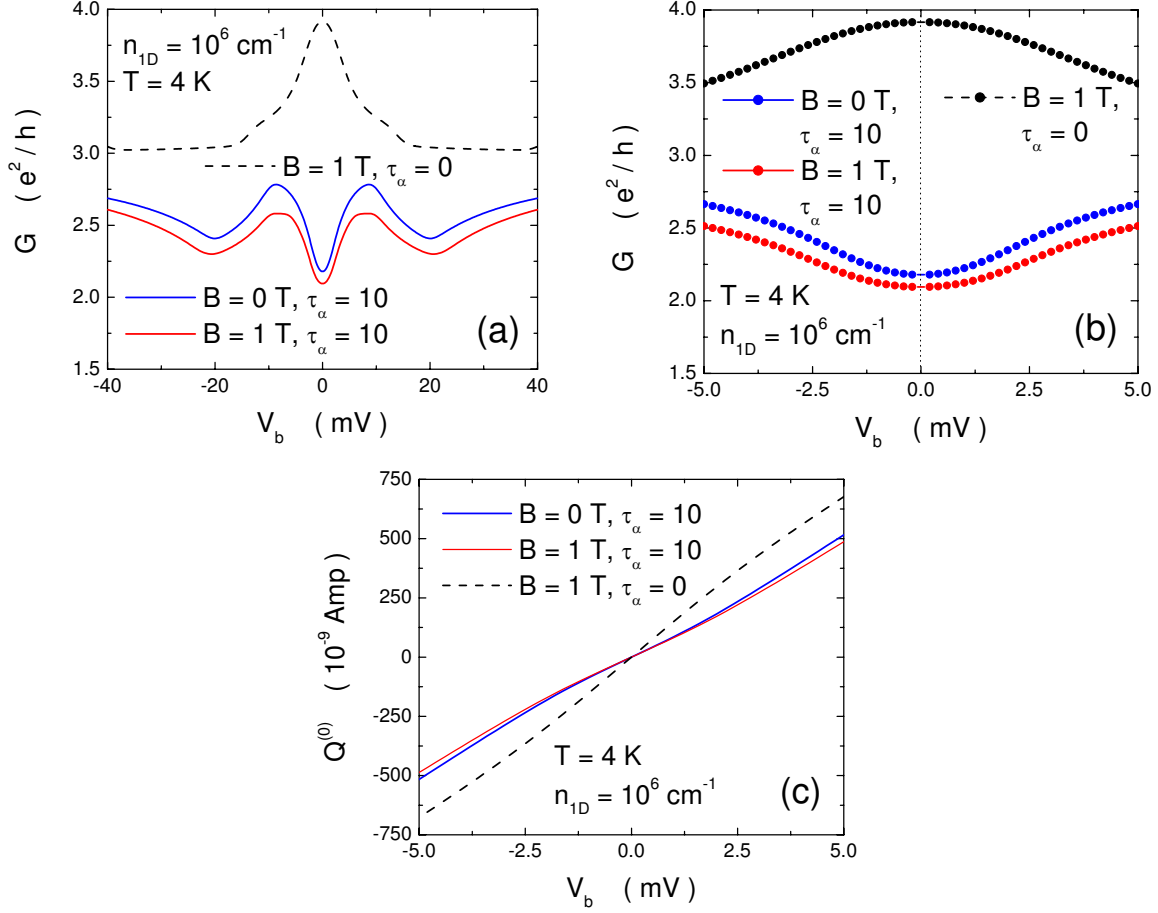


FIG. 4: (Color online) Calculated (a) G , (b) its blow-out view and (c) charge current $Q^{(0)}$ as functions of the bias voltage V_b for $\tau_\alpha = 10$, $B = 0$ T (blue solid curves), $\tau_\alpha = 10$, $B = 1$ T (red solid curves), and $\tau_\alpha = 0$, $B = 1$ T (black dashed curves). Here, $T = 4$ K and $n_{1D} = 10^6 \text{ cm}^{-1}$. The vertical dotted line in (b) indicates the position for $V_b = 0$.

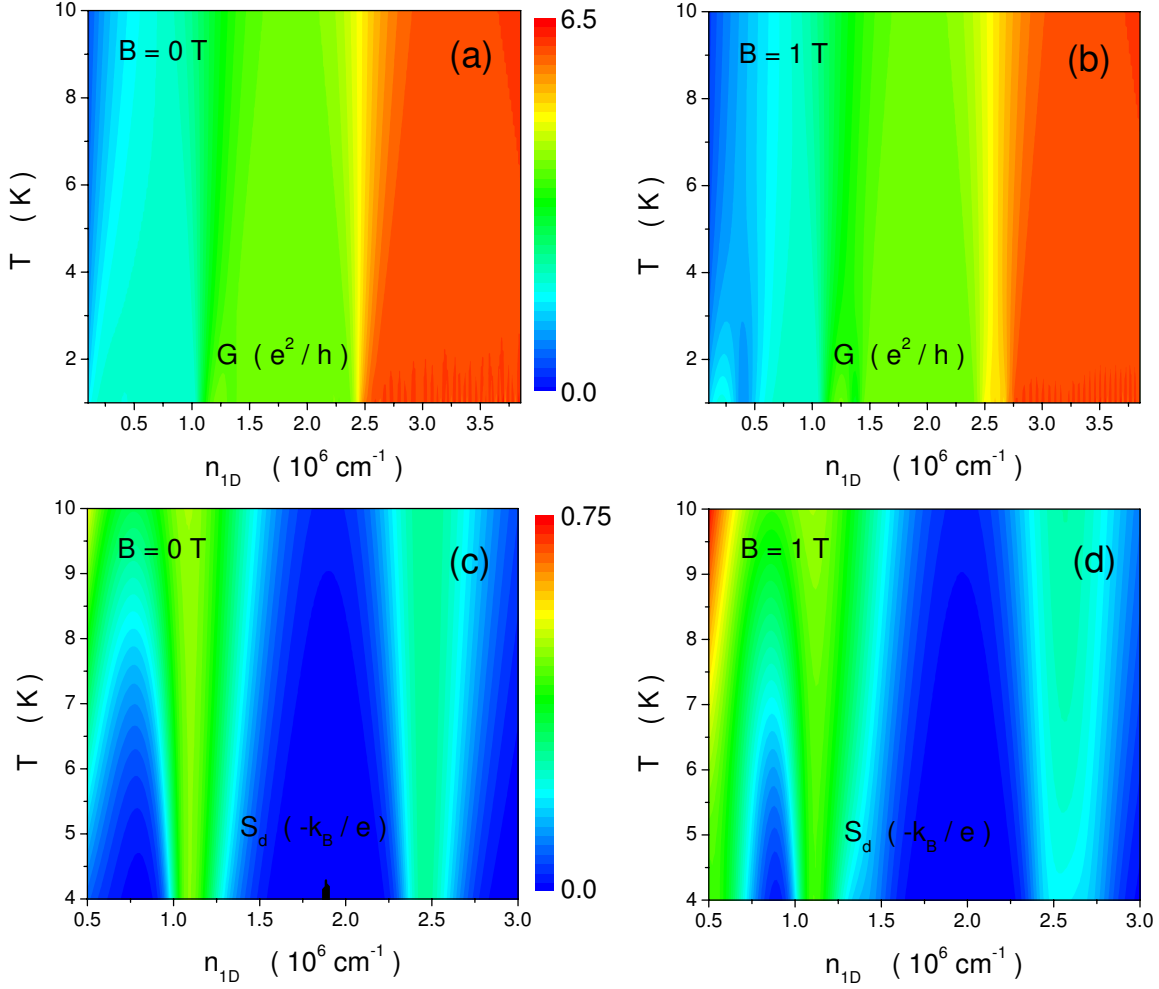


FIG. 5: (Color online) Contour plots of G [in (a) and (b)] and S_d [in (c) and (d)] as functions of n_{1D} (horizontal axis) and T (vertical axis) for $B = 0 \text{ T}$, in ((a) and (c)) and $B = 1 \text{ T}$ ((b) and (d)). Here, $V_b = 0.1 \text{ meV}$ and $\tau_\alpha = 10$. The color scale of G in (a) and (b) varies from 0 (blue) to 6.5 (red), whereas that of S_d in (c) and (d) varies from 0 (blue) to 0.75 (red).

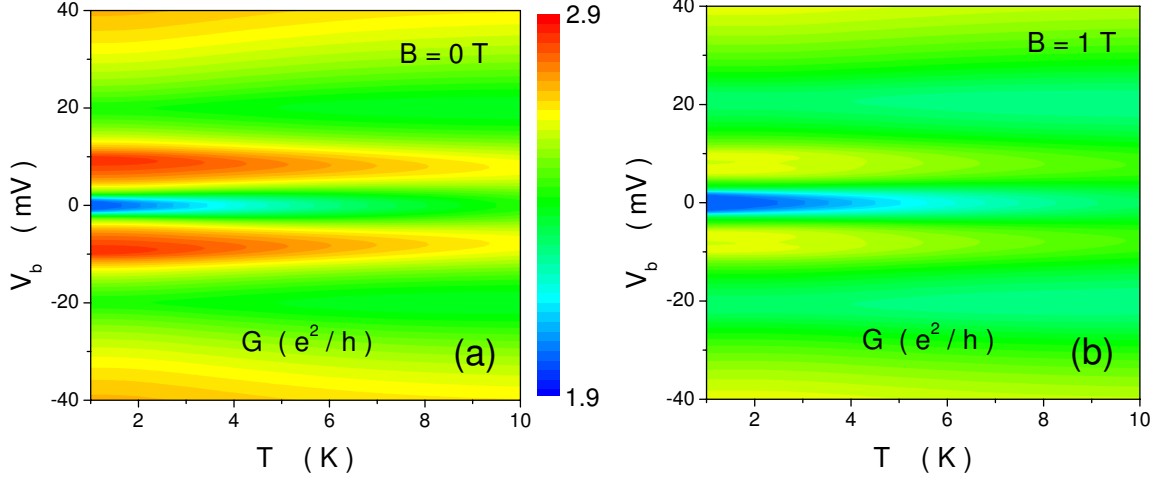


FIG. 6: (Color online) Contour plots of G as functions of T (horizontal axis) and V_b (vertical axis) for (a) $B = 0$ T and (b) $B = 1$ T. We chose $n_{1D} = 10^6 \text{ cm}^{-1}$ and $\tau_\alpha = 10$. The color scale for G in (a) and (b) varies from 1.9 (blue) to 2.9 (red).

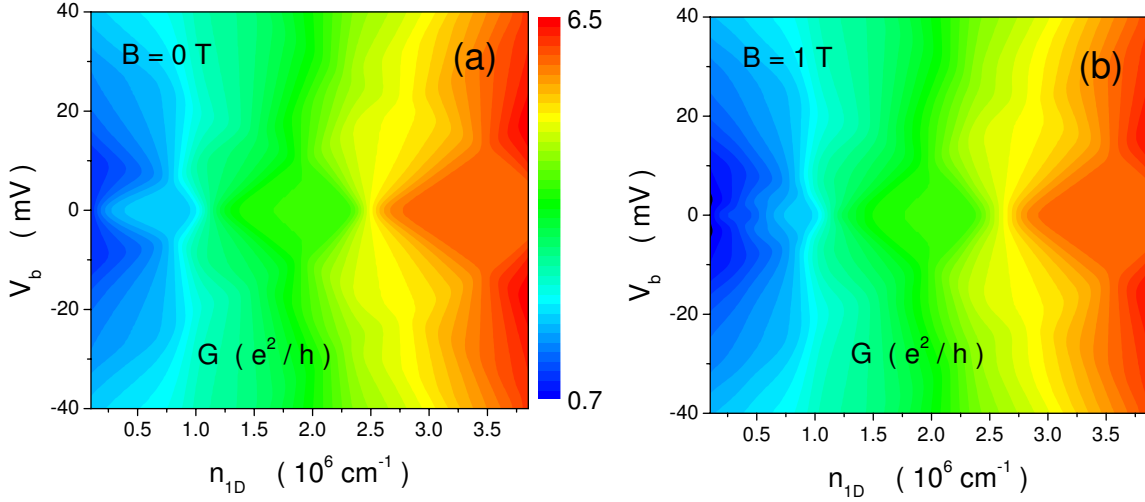


FIG. 7: (Color online) Contour plots of G as functions of n_{1D} (transverse) and V_b (vertical) for $B = 0$ T [in (a)] and $B = 1$ T [in (b)]. Here, $T = 4$ K and $\tau_\alpha = 10$. The color scale of G in (a) and (b) is from 0.7 (blue) to 6.5 (red).